Nanoscale Advances

ROYAL SOCIETY OF CHEMISTRY

PAPER

View Article Online
View Journal | View Issue

Cite this: *Nanoscale Adv.*, 2020, **2**, 4591

Understanding the thermal conductivity variations in nanoporous anodic aluminum oxide†

Liliana Vera-Londono, Alejandra Ruiz-Clavijo, Olga Caballero-Calero and Marisol Martín-González *

Anodic porous alumina (AAO) templates, also known as nanoporous anodic alumina (NAA) platforms or membranes, are widely used as templates in nanoscience and nanotechnology. During fabrication, characterization, or device performance, they are sometimes exposed to heat treatments. We have found that the thermal conductivity of AAO is strongly dependent on the temperature at which the sample is exposed, showing a certain variation even at very low temperatures, such as 50 °C. Because of this, we have performed a study of the thermal conductivity (k) variation for different AAO templates using 3ω-Scanning Thermal Microscopy (3ω-SThM) as a function of the annealing temperature. The AAOs studied in this work were produced in the most common electrolytes – sulfuric, oxalic, and phosphoric acids, and heated from RT up to 1100 °C. To explain these variations in an in-depth and enlightening manner, structural characterization of the different nanoporous aluminas has been performed. It is shown that even at low temperatures, below 100 °C, the AAOs lose water, which explains the reduction of their thermal conductivity. The minimum value of thermal conductivity can be found for AAO samples prepared in sulfuric acid and heated at 100 °C (0.78 ± 0.19 W m^{-1} K^{-1}), which corresponds to a 50% reduction from the original value. It has also been found that for AAO annealed above 950 °C, the variations in the thermal conductivity are mainly related to phase transitions from amorphous to crystalline alumina and gas evolution of CO_2, or SO_2 and SO, depending on the electrolyte used during the anodization. This is also an indication that the counter ions are trapped inside the alumina template during the anodization process. And, their presence determines the crystallization temperatures at which the different crystalline phases are formed. And so, the variations in thermal conductivity are measured. The thermal conductivity values of the AAO can reach values as high as 4.82 ± 0.36 W m^{-1} K^{-1} for AAO samples prepared in oxalic acid and heated up to 1300 °C. We consider that the understanding of the changes in their thermal conductivity can explain the different values in the thermal conductivity of the AAO template found in the literature and draw some attention to the importance of the history of the AAO platforms that are to be used or measured, since it may change the final thermal properties of the template or device.

Received 15th July 2020
Accepted 10th August 2020

DOI: 10.1039/d0na00578a

rsc.li/nanoscale-advances

Introduction

Nanoporous anodic aluminum oxide (AAO) membranes are very popular and widely used in nanoscience and nanotechnology. Due to their easy manufacturing and size tailoring, the use of AAO membranes is an elegant nanostructuration approach. And it is recognized as an alternative to more sophisticated and expensive methods currently used in nanofabrication.

These AAO membranes are applied in very different ways such as the template-assisted synthesis of high-density arrays of 1D nanomaterials (such as nanowires,[1] nanotubes,[2,3] nanorods,[4,5] segmented nanowires,[6,7] *etc.*), or 3D interconnected nanostructures,[8,9] as masks[10] for preparing nanodots or nanorod arrays or nanopatterned substrates,[11–13] and as substrates to deposit different materials on their surfaces and obtain nanohole or antidot arrays[14] or "holey" films.[15,16] These structures have applications in many fields, such as catalysis,[4,17,18] biology and medical applications,[19,20] optical sensors,[21] magnetism,[7,14,22] spintronics,[6] and thermoelectricity,[23] to cite some.

When AAO membranes are used in many cases they are exposed to low-temperature heat treatments either during the nanostructure fabrication, when using techniques such as metal deposition,[8] thermal evaporation, sputtering,[16] melt infiltration,[24–26] *etc.* or during the post-processing, where fabricated nanowires or nanotubes must be heated to crystallize them or during their characterization, such as the fabrication of lithographically designed contacts where the resists have to be

Instituto de Micro y Nanotecnología, IMN-CNM, CSIC (CEI UAM + CSIC), Isaac Newton, 8, E-28760, Tres Cantos, Madrid, Spain. E-mail: marisol.martin@csic.es

† Electronic supplementary information (ESI) available. See DOI: 10.1039/d0na00578a

cured, or when the AAOs are exposed to laser beams for long-times, *etc.* In these processes, the temperature of the AAOs can rise from tens to hundreds of degrees for different extents of time.

It is generally assumed that AAO membranes do not change their chemical and physical properties when exposed to low temperatures. But in the literature, there is a wide range of reported values for the thermal conductivity of AAOs (see Table 1), with values ranging from 0.5 to 1 W m^{-1} K^{-1} measured by a steady-state method at room temperature (RT) for AAO membranes fabricated in sulfuric acid when varying the anodizing temperatures,[27] or higher values, such as 1.3 ± 0.1 W m^{-1} K^{-1} at room temperature for sulfuric acid fabricated membranes when measured by the 3ω-technique, the photothermal method[28] or the laser flash method.[29] In the case of oxalic anodized AAOs, values between 0.63 W m^{-1} K^{-1} and 1.33 W m^{-1} K^{-1} were measured by the steady-state technique at RT when the anodizing temperature varied.[27] The range for thermal conductivity at RT for phosphoric anodized AAOs goes from 1.32 W m^{-1} K^{-1} when measured by the photoacoustic technique[30] to 1.9 W m^{-1} K^{-1} when similar AAOs were measured by 3ω-SThM.[31] Sometimes these discrepancies in the values have been interpreted as compositional changes or attributed to different grain boundaries in the non-ordered porous nanostructures.[37] Moreover, when the AAO membrane is heated at high temperatures it crystallizes and the thermal conductivity value of crystallized bulk α-Al_2O_3 can be as high as 30 W m^{-1} K^{-1} at RT.[32]

To explain these discrepancies, in this work, a set of samples was fabricated using the three most used acid solutions (namely, sulfuric, oxalic, and phosphoric) and anodizing conditions. The changes in the thermal conductivity, structure, and crystallization are studied in the as-obtained AAO membranes and after annealing up to 1300 °C. The thermal conductivity of the AAO membranes has been measured by 3ω-Scanning Thermal Microscopy (3ω-SThM), which allows us to characterize this property at the nanoscale. Also, some of the values obtained were cross-checked with the photoacoustic method, obtaining similar thermal conductivity values within the experimental error for both techniques.[42,43] This in-depth study is crucial to shed some light on the variation of the thermal conductivity observed in the literature for porous alumina and to determine the effect of heat treatment (even at very low temperatures) on its properties. Finally, since one of the properties that affects the performance of devices is heat dissipation, it is quite relevant to determine any possible changes on the porous alumina membrane upon heating.

Experimental methods

Fabrication of the AAOs

Three different sets of AAOs have been used in this study: anodized in sulfuric (H_2SO_4), oxalic ($H_2C_2O_4$), and phosphoric (H_3PO_4) acids, which will be named sulfuric-AAOs, oxalic-AAOs, and phosphoric-AAOs, respectively. The first two were lab-made, being prepared from 99.999% aluminum foil of 0.5 mm in thickness (Advent Research Materials). The aluminum foil was cut in discs of 30 mm approximately and then cleaned successively in acetone, water, isopropanol, and ethanol for 4 minutes in an ultrasonic bath. Next, they were electropolished in a solution of ethanol and perchloric acid 3 : 1 at 20 V for 4 minutes. The fabrication of the membranes was performed *via* a two-step anodization process, as it is described in ref. 30. In brief, it consists of a first anodization step where an aluminum oxide layer is created on the surface. This is carried out for 24 hours to achieve the ordering of the pores, followed by the removal of this first anodic alumina film by chemical etching in phosphoric acid 6% wt, chromic oxide 1.8% wt and deionized water. Then, a second anodization step is carried out under the same experimental conditions for 15 to 20 hours. For the sulfuric-AAOs, the anodization bath consisted of 0.3 M sulfuric acid in deionized water, applying 25 V between the aluminum and a counter electrode made of platinum mesh while maintaining the anodization bath between 1 and 3 °C. In this way, AAOs with an ordered porous structure with a diameter of around 25 nm were produced. In the case of oxalic acid, the anodization voltage was 40 V in a 0.3 M oxalic bath, with the same bath temperature, obtaining in this case a porous structure of around 35 nm in diameter. In both cases, once the two-step anodization process was performed, the remaining aluminum substrate was etched using a solution of $CuCl_2$/HCl. Due to this reaction being exothermic, it has been performed in a 200 ml beaker with only the aluminum part in contact with the solution. During this process, the alumina template could be heated at low temperatures because of the exothermic reaction that is taking place. This etching step can affect the final water content in the AAO at RT, thus explaining the difference observed by TGA/DSC water content loss between our AAOs and those found in the literature, as in ref. 44, and therefore it is important to know if it has been performed and in which conditions. This is also a clear source of variation in the actual values of the thermal conductivity of the alumina since some alumina templates will have more water inside than others. This would change the thermal conductivity value at room temperature and its variation from RT to 100 °C. Finally, the barrier layer was dissolved in 10% wt H_3PO_4 at 30 °C, obtaining a nanoporous membrane. The phosphoric-AAOs were commercial membranes from the company Whatman®, with pores around 200 nm in diameter. All the measured AAO membranes presented a total thickness between 35 to 60 μm.

Annealing processes

The annealing process was performed in a tubular oven (Model ST115020 from Hobersal equipped with an external temperature controller). A second thermocouple was placed inside the oven with the samples to read the actual temperature at which the samples were being heated. The samples were introduced at room temperature and then heated with a heating rate of 10 °C per minute up to the desired temperature (50, 100, 150, 200, 600, 950 and 1100 °C), where they were kept for 1 hour, and then they were cooled down to ambient temperature. The samples heated up to 1300 °C were made in different equipment, heated with the same rate of 10 °C per minute, and cooled down after

Table 1 Summary of some of the thermal conductivity values of AAOs found in the literature. The type of sample, the technique used, and the temperature range of the measurements can be found

Sample type	Thick (μm)	Porosity (%)	Measurement technique	Temp. measure (K)	Thermal conduct ($W\ m^{-1}\ K^{-1}$)	Comments	Ref.
Bulk alumina			Five different techniques	RT-2073	~33 to 6.28	Minimum K obtained between 1600–1900 K	33
Bulk alumina			Steady-state flow method	3–1000	10 000 to 10		32
α-Al_2O_3	5100		Longitudinal heat-flow	~300 ~330 ~360	~33.33 ~28.57 ~25	Pure α-Al_2O_3	34
Thick anodized aluminum coating	~60		Transient heat-flow	RT	0.7	Anodic oxidation in sulfuric acid	35
Thick anodized aluminum coating	~60		Transient heat-flow	RT	1.3	Anodic oxidation in oxalic acid	35
Alumina film on silicon by electron beam	0.5 to 4		Steady-state	RT	0.72	Electron beam evaporation	36
Free-standing amorphous alumina	0.14		Steady-state	90 to 350	0.5 to 2 1.6 at RT	Non-porous Al_2O_3, anodization in ammonium citrate	37
Free-standing amorphous alumina	0.14		Steady-state	90 to 680	~0.6 to 2.5 ~1.8 at RT	Calculated with minimum K	37
α-Al_2O3			3ω method	80 to 400	~0.6 to 1.8 ~1.5 at RT	Produced by PVD (DC magnetron sputtering)	38
α-Al_2O3			3ω method	80 to 400	~0.3 to 1.4 ~1.15 at RT	Produced by PVD (RF magnetron sputtering)	38
α-Al_2O_3 κ-Al_2O_3, coating	13		3ω method	80 to 600	~35 to 15 ~30 at RT ~15 to 6 ~8 at RT	Produced by CVD	39
Porous alumina nanostructures α-Al_2O_3	1340	~3	Laser flash	298.15 to 1473.15	~3.5 to 5 at RT ~6.5 at 1073 K	Sintering $T > 1300$ K (FD1/3 sample in the paper)	40
Thick anodic alumina membrane	55	~30	3ω method & photothermal	80 to 300	0.54 at 80 K to 1.3 at RT	Anodic oxidation in sulfuric acid	28
Anodic alumina film	1.4 to 5	~30	Laser flash	220 to 480	1.22 to 1.71 1.3 at RT	Anodic oxidation in sulfuric acid	29
Aluminum anodic oxide layer (different anodization T_s)	~15 to 80	~14 to 60	Steady-state technique	RT	0.53 to 1.01	Anodic oxidation in sulfuric acid	27
Aluminum anodic oxide layer (different anodization T)	~15 to 80	~10 to 30	Steady-state technique	RT	1.31 to 1.62	Anodic oxidation in oxalic acid	27
Aluminum anodic oxide layer (different anodization T)	~15 to 80	~10 to 35	Steady-state technique	RT	0.82 to 1.12	Anodic oxidation in mixed sulfuric and oxalic acids	33
Commercial aluminum anodic oxide membranes		41	3ω-SThM	RT	1.9	Anodic oxidation in phosphoric acid	31
Aluminum anodic oxide membranes (pores of 350, 220 and 120 nm)			3ω-SThM	RT	1.38	Anodic oxidation in phosphoric acid	41
Aluminum anodic oxide membranes (different conditions)		~10 to 60	Photo-acoustic technique	RT	1.07 sulfuric 1.32 oxalic and phosphoric	Anodic oxidation in sulfuric, oxalic, and phosphoric acids	30

the maximum temperature was reached. Given that it has been reported that for higher temperatures the phase transformation takes place in shorter times,[45] we have also included them in our study. Finally, AAOs without any thermal treatment (which we will call room-temperature, RT, samples) were also included for comparison.

Characterization techniques

The characterization of the samples was carried out with a Scanning Electron Microscope (SEM) VERIOS 460 from FEI. Differential Scanning Calorimetry (DSC), Thermogravimetry (TGA), and mass spectroscopy were performed in a DSC/DTA/TGA module Q600 from TA Instruments, which can conduct simultaneously DSC and TGA from ambient temperature to 1500 °C (from the SIdI-UAM service), with a nitrogen gas flow of 100 ml per minute. The measurements were performed in a dynamic regime while applying a thermal ramp of 10 °C min^{-1}. The system also has a mass spectrometer that can give information on the gasses released by the sample. The crystalline structure of the AAOs has been studied with an XRD Philips X'Pert four circles diffractometer with Cu K_α radiation. Density measurements were carried out *via* the Archimedes method, using an analytical balance XSE105DU from Mettler Toledo. Raman spectra were recorded with a confocal Micro-Raman spectrometer LabRAM 800 from Horiba Jobin Yvon with an excitation wavelength of 532 nm. The thermal conductivity of some membranes was also measured by the photoacoustic method for metrology purposes. More detailed information can be found in ref. 30. This method is based on detecting the phase-shift between periodical heating of the sample with a pulsed laser and the acoustic waves which are generated due to this heating and propagated inside a specially designed photoacoustic cell.

The topographic images of the AAOs at room temperature were obtained with an Atomic Force Microscope (AFM) from Nanotec Electronica, operated in contact mode. To obtain the thermal images, the AFM was operated as scanning thermal microscopy (SThM) in 3ω mode, scanning the surface of the samples with a sharp temperature-sensing tip,[46] which has to be previously calibrated (see the ESI† for further details). From this calibration, we obtain a heat exchange radius of 250 nm. In brief, this mode involves sending a modulated voltage at a frequency ω to the tip. As a result of these temperature changes, the resistance of the tip also changes, and these changes can be recorded thanks to a lab-made Wheatstone bridge. Analyzing the signal obtained at the third harmonic (3ω) of the original modulated voltage, it is possible to acquire the thermal profile of the studied sample, and, after applying an effective medium theory to take into account the contributions of the pores and the skeletal alumina (see the ESI for further details, and Fig. S2 and S3†) the thermal conductivity coefficient can be extracted.[31,47] The probes used in this 3ω-SThM setup were micro-fabricated Pd/Si_3N_4 from Bruker®. Data acquisition was performed using a lock-in amplifier from Zurich Instruments. The data were obtained and processed using the WSxM software.[48] It is important to highlight that in the case of SThM measurements, there is no need for previous preparation of the sample or minimum area. So the thermal conductivity of the samples is not affected by any post-treatment of the AAO membranes.

Results and discussion

Thermal conductivity was obtained at room temperature for the different AAO-membranes that were previously annealed, using the 3ω-Scanning Thermal Microscopy technique (3ω-SThM). In Fig. 1 the obtained images (topography, 3ω, and 1ω) of oxalic-AAOs treated at different temperatures are shown, as an example. The images were recorded for different AAOs as obtained and annealed at different temperatures up to 1300 °C. For each of the samples measured along with the topographical image, we obtain the 1ω signals, which allow us to extract qualitative information on the temperature, and the 3ω signals, which allow as to quantitatively measure the thermal conductivity. These images can be obtained with high sensitivity thanks to a recently improved lab-made electrical circuit connected to the thermal tip, which also gives a better resolution for the first and third harmonic of the signal. The tip has been calibrated similar to previous studies[46,49] (see the ESI†). As a result of the calibration, we have found the thermal exchange radius of our tip to be 250 nm.

Just by looking at the images in Fig. 1, it can be observed that the as-obtained membrane has a different temperature distribution (Fig. 1c) from the samples heated at 100 °C. As can be observed in Fig. 1f, the image presents some hot spots with a local change of their thermal conductivity. This is an indication that something is happening at the nanoscale inside the AAO membrane even at 100 °C. These observed variations are of importance to understand the disagreements in thermal conductivity values found in the literature when measuring similar AAO membranes. Furthermore, the fact that each measuring technique may need different post-processing of the AAO membrane that can be associated with heating processes should be taken into account.

It is interesting to observe that although the thermal exchange radius is 250 nm for the 3ω images, higher resolution can be achieved in the 1ω images, but it cannot be quantified. But it allows hinting that the thermal conductivity must be slightly different between the so-called inner and outer layers of the AAO membranes. The outer layer is the region next to the pore channel walls, which has more anion contamination from the electrolyte, while the inner layer is a higher purity alumina region (the approximate limit of both regions is marked with a dashed line in Fig. 1d and h). So it makes sense that they have different thermal conductivities since they have different chemical compositions. The fact that we can observe differences between both layers is interesting because it denotes the high resolution we can achieve in 1ω. It is also interesting to note in Fig. 1 that by heating, the inner and the outer AAO regions behave differently. To better show this variation, the AAO between the pores is amplified in Fig. 1d, h, and l. Finally, in Fig. 1i the images of the oxalic-AAO membrane annealed at 1100 °C are shown. One interesting feature is that the pore size

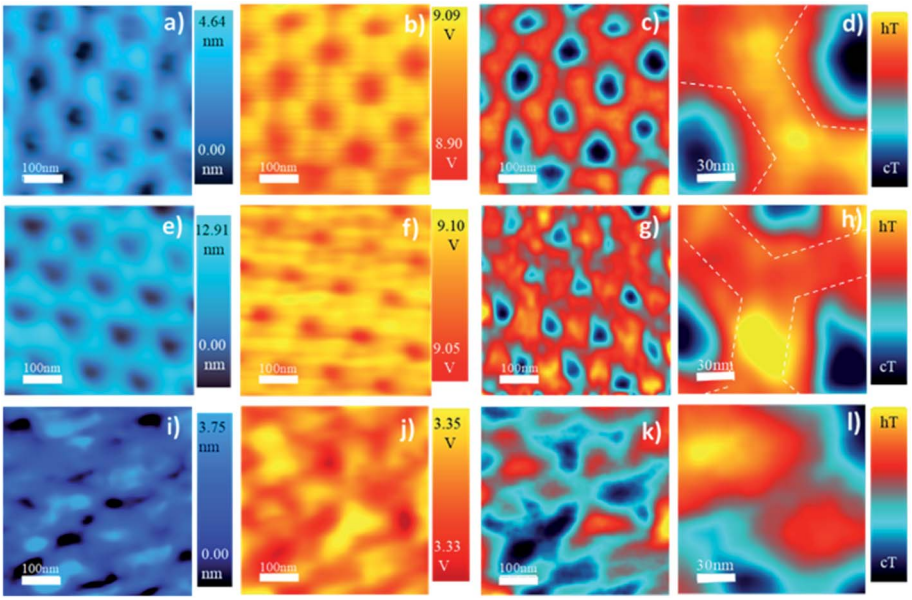

Fig. 1 Oxalic-AAO membranes: topographic images of (a) at RT, (e) after annealing at a temperature of 100 °C, and (i) at 1100 °C. 3ω SThM images of (b), (f), and (j) at RT, 100 °C and 1100 °C, respectively. Voltage signal images at 1ω of (c), (g), and (k) at RT, 100 °C, and 1100 °C, respectively. In the scale bar of 1ω, -hT – means hot temperature and – cT- stands for cold temperature. Images (d), (h), and (l) are the zoom-in of the 1ω images to highlight the changes in the outer and inner regions of the AAO membrane, where the dashed lines mark approximately the limits of the outer layer, which is found between the lines and the pores, and the inner layer.

is bigger, which means that the AAO composition must have changed. It can also be observed that the thermal conductivity of the AAO membrane is strongly modified (see the scale in *V* of Fig. 1b, f, and j).

The thermal conductivity values obtained for the different AAO membranes in the out-of-plane direction are shown in Fig. 2. Changes in the thermal conductivity from as low as 0.78 ± 0.19 W m^{-1} K^{-1}, in the sulfuric-AAO without any thermal treatment to as high as 4.82 ± 0.36 W m^{-1} K^{-1} for an oxalic-AAO annealed at 1300 °C, over six times higher, can be observed. To discuss the results, we have divided the graph into three sections according to their thermal conductivity trend.

In the first low-temperature region (up to ~200 °C) a reduction in the thermal conductivity is observed followed by an increase. This reduction is more noticeable for the samples produced in sulfuric acid solution (sulfuric-AAO). In these samples, a reduction in thermal conductivity is observed from 1.24 ± 0.12 W m^{-1} K^{-1} at room temperature (RT) to 1.09 ± 0.12 W m^{-1} K^{-1} when the sample is heated up to 50 °C, and to 0.78 ± 0.19 W m^{-1} K^{-1} when heated at 100 °C (almost half of the value measured in the as-prepared samples). This is an interesting result since the thermal conductivity of the porous alumina membranes can be reduced by just heating the samples at such very low temperatures <100 °C. This behavior is also followed by the AAO-oxalic samples, but with a lower reduction in the thermal conductivity (from 1.41 ± 0.17 at RT to 1.26 ± 0.24 W m^{-1} K^{-1} at 100 °C). Finally, in the case of the phosphoric-AAO, the minimum value is reached at annealing temperatures around 150 °C. And the thermal conductivity, in this case, varies from 1.44 ± 0.11 at RT to 1.22 ± 0.17 W m^{-1} K^{-1} at 150 °C. This reduction of the thermal conductivity upon heating at such low temperatures can explain the variability of the thermal conductivity in the literature, as shown in Table 1, since some of the measurement techniques need sample preparation, such as the deposition of a metal layer, which can heat the sample to those temperatures very easily.

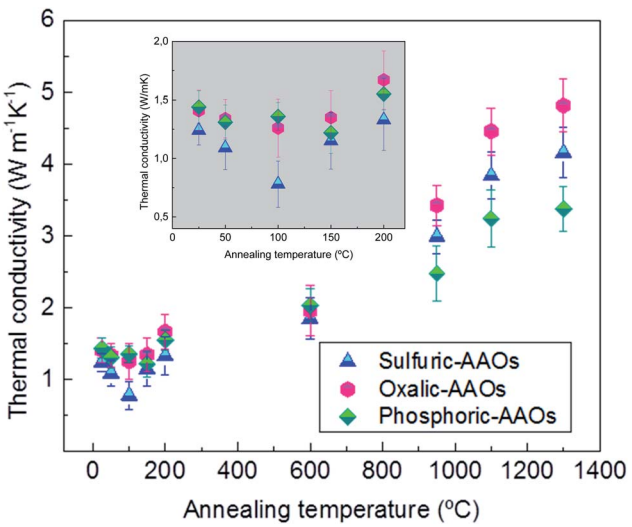

Fig. 2 Thermal conductivity was obtained at room temperature for different AAO samples previously annealed, using 3ω-scanning thermal microscopy; blue triangles represent sulfuric-AAOs, pink hexagons represent oxalic-AAOs, and green diamonds represent phosphoric-AAOs. Thermal conductivity values and the associated errors are shown in Table S1 of the ESI.† The insert, in grey, shows a zoom of the values between RT and 200 °C.

A second region, between temperatures over 200 to 600 °C, is characterized by the thermal conductivity of the AAO membranes to be around 2 W m^{-1} K^{-1}, with differences in the thermal conductivity between the different membranes that stay within the error limit of the measurement technique.

And, a third region is observed, in which the thermal conductivity of the different membranes starts to increase again, reaching values of thermal conductivity of 4.16 ± 0.35 W m^{-1} K^{-1} for sulfuric-AAO, 4.82 ± 0.36 W m^{-1} K^{-1} for oxalic-AAO, and 3.38 ± 0.32 W m^{-1} K^{-1} for phosphoric-AAO when heated up to 1300 °C.

To understand the process that is involved in the variation of the thermal conductivity at different temperatures, we have performed TGA–DSC-mass spectroscopy for the three types of samples to analyze: the weight loss, if the process is endo- or exothermic, and which gas is released during each particular process (see Fig. 3). This analysis has been coupled with X-ray diffraction analysis (shown in Fig. 4), and Raman spectroscopy (Fig. 5) to understand if there is also a crystallization process associated with those temperatures.

As observed by TGA an initial weight loss between RT and 300 °C takes place in the three types of membranes. The measured weight losses are about 0.8% for sulfuric-AAO, 0.5% for oxalic-AAO, and 1% for the phosphoric-AAO. These initial weight losses are ascribed to the evaporation of water molecules from the AAO membranes, as detected by mass spectroscopy. These H_2O molecules are trapped and absorbed in the AAO membranes during anodization. And, they will leave the membrane at these temperatures. The minimum value of the thermal conductivity also corresponds to a reduction in the measured density of the different AAO-membranes annealed at 100 °C (see Fig. S4 of the ESI†). The density values increase again after annealing at 200 °C, which is also related to the increase of the thermal conductivity seen in this region. This is an interesting result since the composition of the AAO templates is changing at very low temperatures, which can

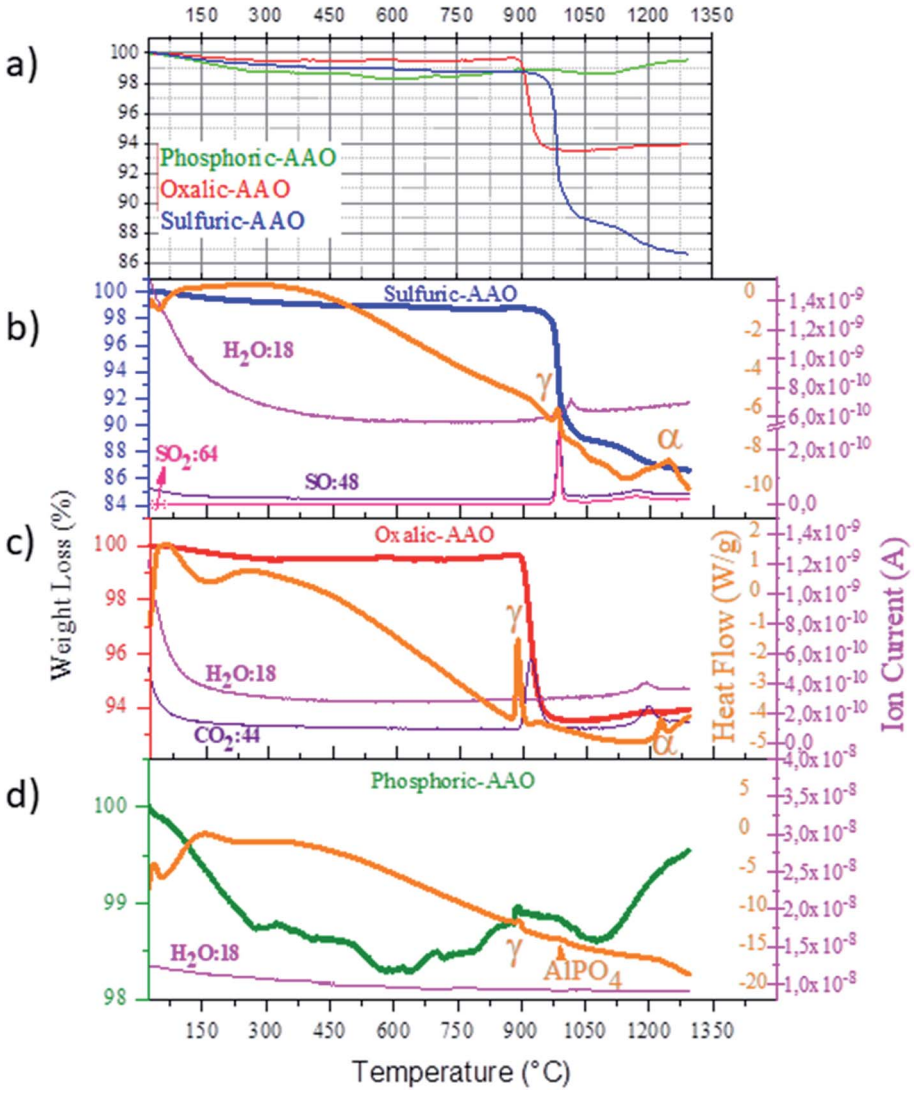

Fig. 3 (a) Comparison of the weight loss of all the AAO membranes. Percentage of weight loss – TGA-, heat flow – DSC-, and mass spectroscopy results of the (b) sulfuric-AAO, (c) oxalic-AAO, and (d) phosphoric-AAO.

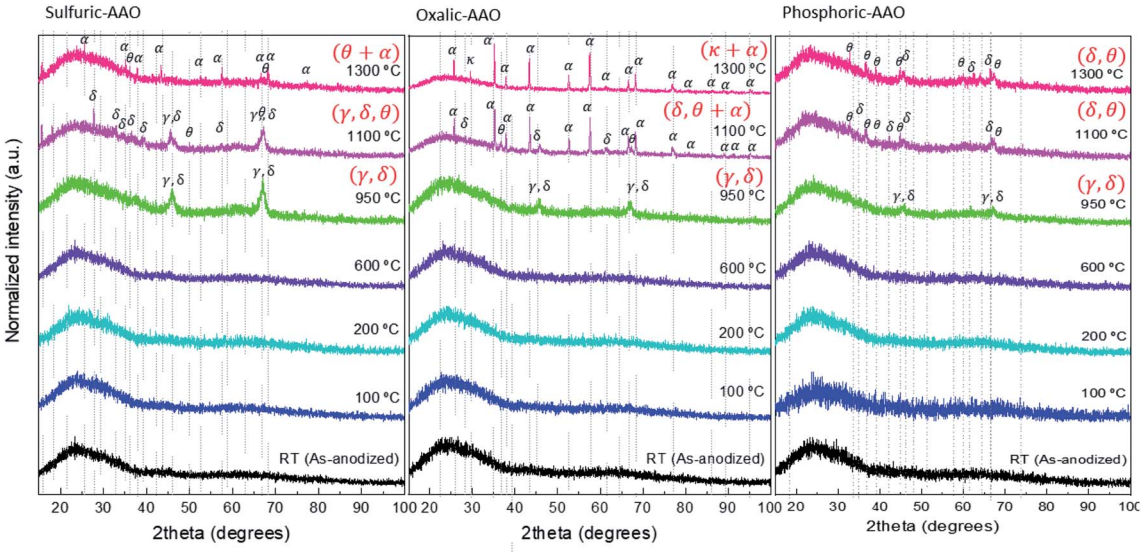

Fig. 4 XRD diffraction patterns measured at room temperature of the AAO samples of this study. The ordering of the graphs is from the left to right sulfuric-AAOs, oxalic-AAOs, and phosphoric-AAOs.

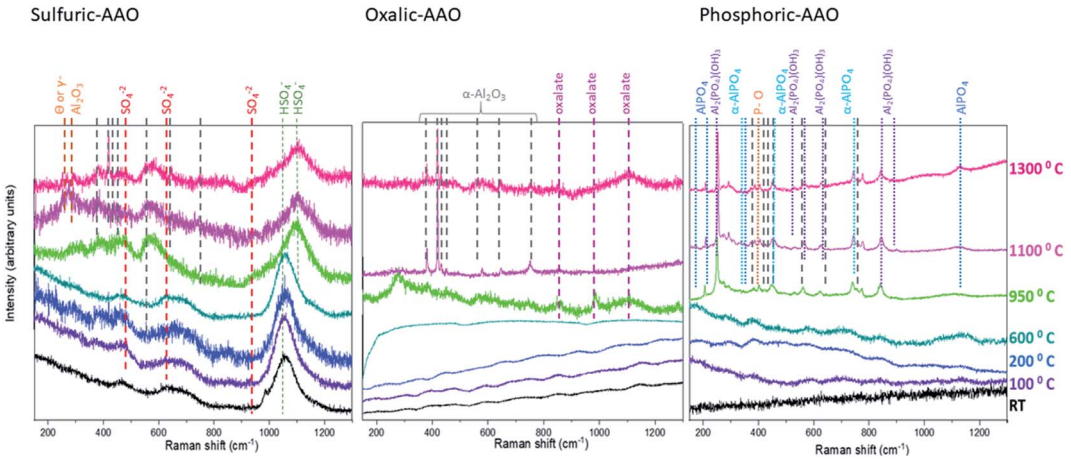

Fig. 5 Raman spectra measured at room temperature of the AAO samples of this study (from left to right: sulfuric-AAOs, oxalic-AAOs, and phosphoric-AAOs). The vibrational modes associated with the α-Al_2O_3 phase are marked in grey. All the other identified modes are depicted in the figure with different colors.

explain the variation in thermal conductivity observed in Fig. 2 and in Table 1.

XRD analysis of these samples in the range between 200–600 °C shows that there is not any clear diffraction peak, indicating that the AAOs are still amorphous. It can be assumed that no important crystallization process has started yet in this annealing temperature range, at least detectable by this technique. This behavior explains why the thermal conductivity of the AAO membranes stays in a kind of a plateau with thermal conductivity values around 2 W m^{-1} K^{-1} in that temperature range (Fig. 2).

Finally, for the high-temperature range (above 700 °C) the behavior of sulfuric-AAOs and oxalic-AAOs is again different from that of the phosphoric-AAOs in TGA (Fig. 3). In the cases of sulfuric-AAOs, two main mass-losses, of 10% around 980 °C and 2.1% around 1245 °C, are observed while for oxalic-AAOs a weight loss of 5.7% is found around 890 °C. Both weight losses can be associated with the thermal decomposition of the counter ion trapped in the templates during fabrication in the different acids (which are sulfate and oxalate, for sulfuric-AAOs and oxalic-AAOs, respectively). At those temperatures, there is a gas evolution in the sulfuric-AAO, that loses SO_2 and SO (with molecular masses of 64 and 48, respectively, as identified by mass spectroscopy during TGA measurements) while the oxalic-AAO membranes lose CO_2 (with a molecular mass of 44).

The loss of trapped counter ions is observed at the same time as the crystallization of alumina, as evidenced by XRD (see Fig. 4). In both cases, sulfuric-AAOs and oxalic-AAOs, the samples annealed at 950 °C start to show diffraction maxima

around 2θ 46° and 67°. So the membranes crystallize as the γ-Al_2O_3 or δ-Al_2O_3 phase (it is difficult to distinguish between these two phases, given that most of their diffraction peaks are common, according to JCPDS-ICDD 00-029-1486 and JCPDS-ICDD 00-016-0394, respectively). This transition is marked with the letter "γ" in Fig. 3. For oxalic-AAOs annealed at 1100 °C, apart from these phases, some maxima corresponding with the α-Al_2O_3 phase start to appear (JCPDS-ICDD 00-043-1484, corundum, hexagonal close-packed structure). In the case of sulfuric-AAOs annealed at 1100 °C, diffraction maxima corresponding to either the γ-Al_2O_3 or δ-Al_2O_3 phase are observed, along with some diffraction maxima related to the θ-Al_2O_3 (JCPDS-ICDD 00-035-0121, monoclinic structure). And the hcp α-Al_2O_3 phase does not appear up to a higher temperature, 1300 °C, for the sulfuric-AAO. This crystallization at higher temperatures than in the case of the oxalic-AAO may be associated with the additional loss of SO_2 and SO around 1160 °C. So, from XRD it can be concluded that the temperatures at which the transition to the hcp α-Al_2O_3 occurs is affected by the counter ion in which the alumina membrane was produced. This transition is shown with the letter "α" in Fig. 3. It is important to highlight also that the degree of phase transformation at 1100 °C is higher for the oxalic-AAOs than for the sulfuric-AAOs at 1300 °C, as detected by XRD. Since the α-Al_2O_3 phase has a higher thermal conductivity, as seen in Table 1, this explains why the thermal conductivity is higher in the oxalic-AAO than in the sulfuric-AAO at 1300 °C.

In the case of the phosphoric-AAO, there is not any important weight loss in that particular range. According to mass spectroscopy, there is not gas evolution either. This is an indication that phosphates trapped inside the alumina membrane do not thermally decompose and stay in the alumina membrane. By DSC, only two small exothermic processes have been observed around 880 and 970 °C, which are related to crystallization, but no other changes are observed above those values. These exothermic processes must be related to the crystallization of the phosphoric-AAO, which starts to be identifiable by XRD, around these temperatures, as shown in Fig. 4. At a 950 °C annealing temperature, the diffraction maxima observed can be associated with the γ-Al_2O_3 or δ-Al_2O_3 phases, as in the previous samples. Then, for the phosphoric-AAO annealed at 1100 °C, the peaks were found to correspond to δ-Al_2O_3 and θ-Al_2O_3. And, different from the sulfuric-AAO and the oxalic-AAO, there is not a phase transition to α-Al_2O_3 even after thermal treatments at 1300 °C. Again this behavior can explain not only why we observed an increase in thermal conductivity at 1000 °C in the phosphoric-AAO (due to crystallization) but also why the thermal conductivity in the range between 1100 and 1300 °C seems to reach another plateau, 3.24 ± 0.38, and 3.38 ± 0.32 W m^{-1} K^{-1}, respectively. However, it is not the case for the sulfuric-AAO that goes from 3.84 ± 0.33 at 1100 °C to 4.46 ± 0.32 W m^{-1} K^{-1} at 1300 °C or the oxalic-AAO that goes from 4.16 ± 0.35 at 1100 °C to 4.82 ± 0.36 W m^{-1} K^{-1} at 1300 °C (see Fig. 2), where the transition to the α-Al_2O_3 phase is observed.

The Raman spectra of the three sets of samples (Fig. 5) confirm both the different phase transitions observed by XRD and the gas evolution detected by TGA–DSC mass spectroscopy, which were comparable to those discussed in previous studies on similar samples,[44,50] and added some further details in the crystallization route followed.

For sulfuric-AAOs from RT to 600 °C annealing temperatures, the Raman spectra show only vibrational modes corresponding to sulfur compounds, like those associated with SO_4^{2-} (located at 451 cm^{-1} (ν_2), 626 cm^{-1} (ν_4) and 984 cm^{-1} (ν_1)[51]). These modes cannot be found for samples annealed above 950 °C, and from TGA–DSC it has been seen that these trapped counter ions have been thermally decomposed at 980 °C, and thus, are not present above this temperature. Another vibrational mode, clearly visible from RT is that associated with HSO_4^-, around 1050 cm^{-1} (ν_s), which is maintained until the sample is annealed at 950 °C, where it changes to a different HSO_4^- mode, namely a ν_3 vibration centered at 1100 cm^{-1},[52] and decreases in intensity. This coincides with the gas evolution of thermal decomposition of SO_2 and SO in this range, and the faint intensity of this vibrational mode at the highest temperatures reflects that there is still a residual presence of these defects in the structure, detectable by Raman spectroscopy. This is also confirmed by mass spectroscopy, where a second gas evolution around 1175 °C can be also observed. Although it has to be pointed out that the presence of electrolyte counterion related phases is not detectable by XRD. In the case of the crystallization route of the samples, for those above 950 °C annealing temperatures, other faint peaks associated with the α-Al_2O_3 crystallographic phase and weak Raman lines, at around 252 and 268.6 cm^{-1} are found. These bands have been discussed in the literature[53,54] as a mark of the coexistence of θ-Al_2O_3 or γ-Al_2O_3 phases with the α-Al_2O_3 phase for AAO-membranes treated above 1000 °C, which is what is obtained by XRD for these samples.

In the case of oxalic-AAOs, the Raman spectra for the samples below 600 °C show important photoluminescence, which is usually associated with impurities or oxygen vacancies.[55] The amount of these impurities seems to be reduced when the sample is annealed at 950 °C (which is above the temperature found in TGA–DSC for the first thermal decomposition of $C_2O_4^{2-}$ to CO_2, ~890 °C). This gas evolution can explain why the photoluminescence is much lower and peaks associated with aluminum oxalate,[51] centered at around 846, 981, 1110, and 1387 cm^{-1} appear weak and as broad bands in the spectra. For lower temperatures, these peaks are present in the sample, but the presence of the photoluminescence band, which is strong and broad, conceal the aluminum oxalate Raman peaks for the laser wavelength used in this study. Nevertheless, when the oxalic-AAO samples are measured with the appropriate wavelength (for instance, an ultraviolet laser with 244 nm wavelength), as was shown in ref. 51, the photoluminescence interference can be avoided and then, the oxalate impurities can be observed, even in the room temperature samples. These oxalate peaks disappear in the sample heated at 1100 °C, where no trace of aluminum oxalate could be identified in agreement with the information from mass spectroscopy. When the annealing temperature is increased at 1100 °C, some α-Al_2O_3 phase vibrational modes start to appear. These α-Al_2O_3

phases or sapphire vibrational modes are located at 378 cm^{-1} (E_g external), 418 cm^{-1} (A_{1g}), 432 cm^{-1} (E_g external), 451 cm^{-1} (E_g internal), 580 cm^{-1} (E_g internal), 645 cm^{-1} (A_{1g}, polarized) and 756 cm^{-1} (E_g internal) as reported in ref. 56. In Fig. 5 their positions are marked by grey dashed lines, and it can be seen that all of them are present and well defined for the sample annealed at 1100 °C.

Finally, the Raman spectra of the phosphoric-AAOs show no distinct peaks for samples with annealing temperatures below 950 °C, again due to the high photoluminescence, as in the previous case, but for higher temperatures, a whole set of peaks appear. But in this case, the gas evolution was not observed. The vibration modes that appear are related to the vibrational modes of P–O bending modes, such as that at 402 cm^{-1}.[57] Also, the α-$AlPO_4$ 336, 440, 566, 650 and 748 cm^{-1} (ref. 58) and the $Al_2(PO_4)(OH)_3$ at 225, 250, 365, 405, 525, 565, 635, 850, and 880 cm^{-1} (ref. 59) could be identified at those temperatures. It is worth mentioning that other studies dealing with phosphoric-AAOs studied with respect to temperature have also shown the presence of $AlPO_4$ even at a temperature of 1450 °C.[44] So, it can be concluded that at these temperatures the trapped phosphates form α-$AlPO_4$ and $Al_2(PO_4)(OH)_3$ which are amorphous according to XRD, in our case. It must be highlighted that no vibrational modes related to the α-Al_2O_3 phase could be identified. This confirms the absence of a complete crystallization of the phosphoric-AAOs into α-Al_2O_3, as seen by XRD, even after annealing treatments at 1300 °C.

To summarize, if one analyzes the results obtained by TGA–DSC-mass spectroscopy, XRD, and Raman spectroscopy for the different regions pointed out in Fig. 2, the following interpretation of the different behaviour of the thermal conductivity can be drawn. In the low-temperature region, up to 200 °C, both XRD and Raman spectroscopy show amorphous structures. The density measurements of the skeletal alumina in this range also show a certain decrease after annealing at 100 °C, followed by an increase for those annealed at 200 °C. Then, the reduction and the increase of the thermal conductivity has to be related to the water evolution detected by TGA–DSC-mass spectroscopy, where the weight loss in water is more evident in sulfuric-AAOs, reaching 6% water loss at 200 °C (which presents the biggest fluctuation in Fig. 2 in this range), and they are also the membranes that show the highest fluctuation in the thermal conductivity values. This behaviour is similar but less strong for oxalic-AAOs (with a value of 4 and 5% in water loss). Finally, the water loss is very low for phosphoric-AAOs, with around 1 and 2% water loss at that temperature, which correlates with a less marked change in the thermal conductivity values for this range.

In the second region, between 200 to 600 °C, the thermal conductivity was stable around a value of around 2 $W\,m^{-1}\,K^{-1}$, and this corresponds to TGA–DSC-mass spectroscopy results showing no special gas evolutions, or crystallization occurring in that range, as observed by XRD and Raman spectra.

In the third region, corresponding to the highest temperatures studied in this work, up to 1300 °C, the TGA–DSC mass spectroscopy results show different decompositions of counter ions trapped in the oxalic- and sulfuric-AAOs, as shown by XRD and Raman spectra that at the temperatures that these counterions start to decompose, these membranes start to crystallize. The transition to the hcp α-Al_2O_3 phase is complete for the oxalic-AAO at 1300 °C, with this membrane being the one that shows the highest thermal conductivity in this range. This can be explained by the α-Al_2O_3 being the alumina phase with higher thermal conductivity among the different Al_2O_3 crystalline phases. Then, the lowest thermal conductivity values in this region correspond to phosphoric-AAOs, which do not show any important weight loss in this range. That is, no gas evolution is detected. This indicates that the phosphates get trapped in the phosphoric-AAOs. And they do not thermally decompose but react with the alumina as observed by Raman spectroscopy. No presence of the high conductivity α-Al_2O_3 phase is detected, even after the highest annealing temperature treatment.

To identify if those gas evolution and crystallization processes have any effect on the morphology of the AAO membranes, SEM images of each of the AAO membranes were obtained after the different temperature treatments and are compiled in Fig. 6. To quantify those changes, the porosity and pore diameter have been analyzed as a function of the annealing temperature (see Table S2 of the ESI†). In all the cases, the SEM images show that the porous diameter does not change up to 950 °C, indicating that the membranes can be useful in different applications in which temperature processes up to this value are involved. For annealings above 950 °C, the porous structure of AAO membranes is slightly modified, as has also been reported in previous studies, for instance, in oxalic-AAOs.[60] Their porosity increases to more than double the value for sulfuric- and oxalic-AAOs. And so does the pore diameter. This can be due to the two processes that were mentioned before for these two types of AAOs in that temperature range: gas evolution and crystallization. It is worth reminding that, for oxalic-AAOs, after annealing at 1100 °C, the α-Al_2O_3 phase is obtained, which has a higher density than the others (as can be also seen in the density plot, Fig. S4 of the ESI†). In the case of phosphoric-AAOs, they do not show any clear morphological change in the pore diameter. This can be explained by the fact that there is no gas evolution and the crystallization of the sample barely starts. Nevertheless, it is important to say that phosphoric-AAOs become buckled or cracked when heated above 700 °C. For the highest annealing temperatures, the SEM images of the phosphoric-AAO show a kind of "whiskers" covering the surface; similar behaviour has been observed in previous studies for the same type of AAOs.[61] This morphological change is seen above 950 °C in this study, as can be observed in the SEM images (Fig. 6f and c). These whiskers are amorphous according to XRD, but we have been able to identify them by Raman spectroscopy as $AlPO_4$ and $Al_2(PO_4)(OH)_3$, see Fig. 5. The formation of these phases can also be identified by DSC. And it is denoted as $AlPO_4$ in Fig. 3. This phase segregation at the top and bottom of the membrane generates a phosphorous gradient concentration though the pores and can explain why these membranes became more brittle than the other membranes. To perform appropriate thermal conductivity measurements as shown in Fig. 2, the samples were polished.

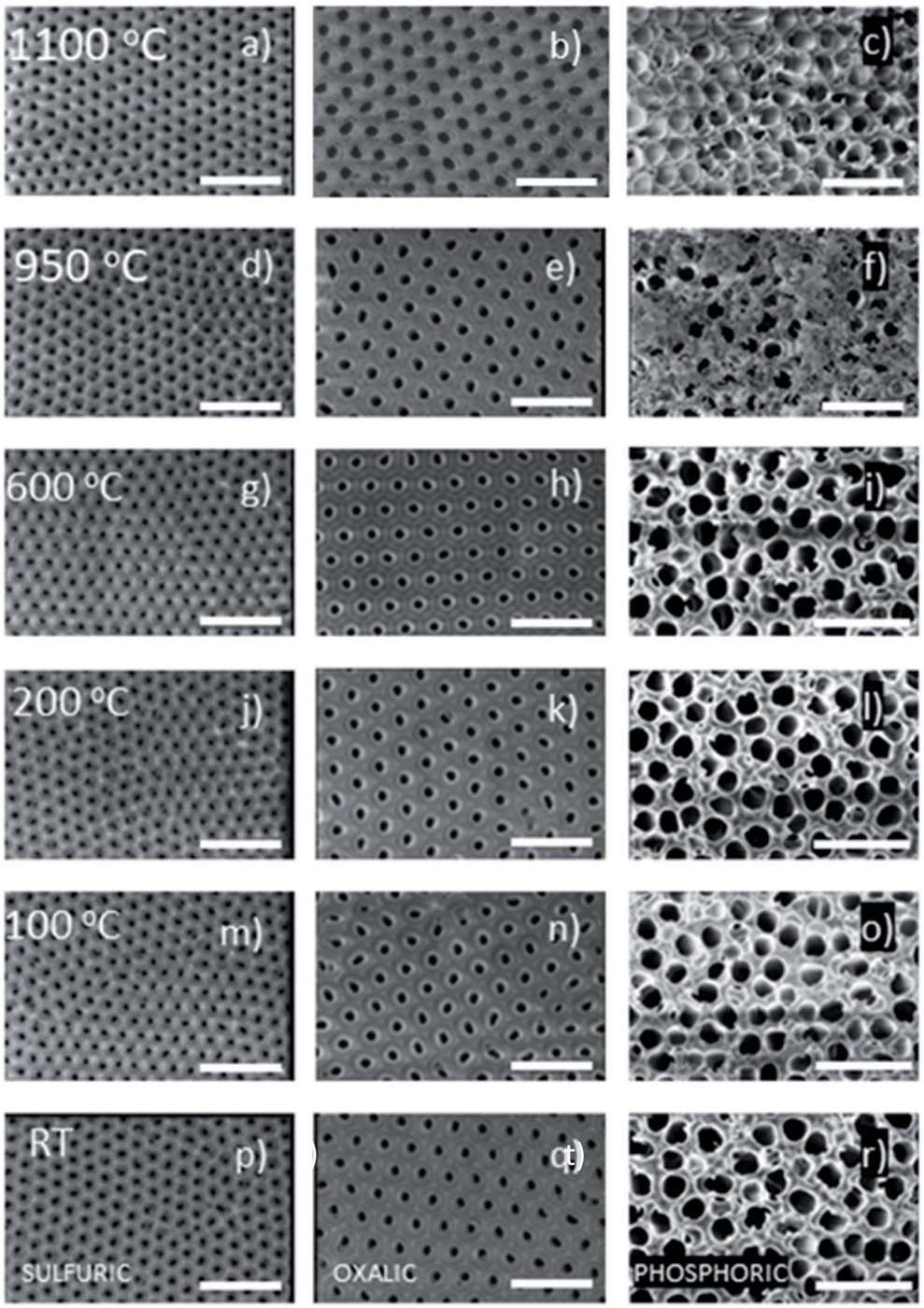

Fig. 6 SEM images of all the AAO samples of the study. Left column, sulfuric-AAOs (a, d, g, j, m, p), center column oxalic-AAOs (b, e, h, k, n, q), and right column, phosphoric-AAOs (c, f, i, l, o, r). The scale bar corresponds to 300 nm for sulfuric-AAOs and oxalic-AAOs; and 1 μm for the phosphoric-AAOs. The images correspond to the AAO membranes after the different annealing treatments: 1100 °C (a–c), 950 °C (d–f), 600 °C (g–i), 200 °C (j–l), 100 °C (m–o) and the untreated ones (p–r).

Conclusions

In this work, we have understood the influence of annealing treatments on the thermal conductivity of different AAO membranes prepared in the most common anodization acids: sulfuric, oxalic, and phosphoric acids. With the information gathered in this work, we can conclude some important results for the scientific community using alumina membranes.

On the one hand, the thermal conductivity of the AAO membranes depends on the acid used in the anodization. This is due to the influence of counter-ions that get trapped inside the outer layer of the alumina during the anodization process.

Therefore, each type of alumina presents a different thermal conductivity value because they are slightly different.

On the other hand, the thermal conductivity of the AAO membranes changes even at very low temperatures (50 °C). This is very important because depending on the thermal conductivity measurement technique, one may need to evaporate metal contacts, or transducers, or cure a photo-resist when carrying out the lithography process, or the samples must be heated by lasers, *etc.* which can generate some heating in the AAO membrane. This heating can produce water evolution from the AAO membrane, which modifies their thermal conductivity. This is of importance for example when determining the thermal conductivity of the nanowires inside AAO membranes. To obtain an accurate value of the nanowires, an empty AAO membrane must be measured under the same conditions and post-treatments as the AAO with the nanowires, to obtain an accurate value of the nanowires, instead of using the values from the literature for untreated AAOs.

Another important conclusion is that the thermal conductivity of sulfuric-AAOs can be reduced to values around 0.7 $W m^{-1} K^{-1}$ upon heating the membrane at 100 °C. This is a good result, for example, if the AAO membrane has to be used in areas in which a low thermal conductivity is of importance, such as in thermoelectrics.

It is also worth noting that the impurities are different depending on the electrolyte used in the anodization process and that they affect the crystallization of the AAO membranes differently. These impurities influence the temperature at which the transformation starts and also the crystalline phases in which the AAO crystallizes. These, of course, have an influence on the value of thermal conductivity of the membranes after different thermal treatments. For example, above 1300 °C the total transformation to a stable hcp α-Al_2O_3 phase happens for oxalic-AAOs, partially for sulfuric-AAOs, and it is not achieved for phosphoric-AAOs.

Therefore, this work provides a better understanding of how thermal conductivity changes in AAO membranes. This is key to understanding the impact that the annealing temperature and the anodization conditions have on the physical, chemical, and structural properties of this oxide. This must be taken into account when applying this type of structure as a self-supporting membrane or coating. These findings could have a great impact on the engineering design of different anodized oxide porous structures, also having a high relevance for the development of thermal transport models for these types of structures.

Finally, this understanding of the change of thermal conductivity in AAOs must be taken into account when using these membranes in real devices. If the membrane is heated up (even at very low temperatures) the thermal conductivity will change, modifying its final performance.

Conflicts of interest

There are no conflicts to declare.

Acknowledgements

The authors would like to thank Mr Pablo Cerviño for measurements with the Photoacoustic Technique performed during his Master Thesis work. We acknowledge the project MAT2017-86450-c4-3-r and CAM18-PRE-IMN-001 fellowship of ARC. We also acknowledge the service from the MiNa Laboratory at IMN, and funding from CM (project SpaceTec, S2013/ICE2822), MINECO (project CSIC13-4E-1794) and EU (FEDER, FSE).

References

1 P. M. Resende and M. Martín-González, Sub-10 nm porous alumina templates to produce sub-10 nm nanowires, *Microporous Mesoporous Mater.*, 2019, **284**, 198–204.
2 S. Kapoor, *et al.*, Synthesis of highly reproducible CdTe nanotubes on anodized alumina template and confinement study by photoluminescence and Raman spectroscopy, *J. Alloys Compd.*, 2019, **809**, 151765.
3 J. Azevedo, *et al.*, Double-walled iron oxide nanotubes *via* selective chemical etching and Kirkendall process, *Sci. Rep.*, 2019, **9**(1), 1–8.
4 M. K. Date, *et al.*, Three-dimensional CuO/TiO_2 hybrid nanorod arrays prepared by electrodeposition in AAO membranes as an excellent Fenton-like photocatalyst for dye degradation, *Nanoscale Res. Lett.*, 2020, **15**(1), 1–12.
5 K. Liu, *et al.*, Plasmonic Au nanorods stabilized within anodic aluminum oxide pore channels against high-temperature treatment, *Nanotechnology*, 2019, **30**(40), 405704.
6 F. Nasirpouri, *et al.*, Geometrically designed domain wall trap in tri-segmented nickel magnetic nanowires for spintronics devices, *Sci. Rep.*, 2019, **9**(1), 9010.
7 S. Moraes, *et al.*, The role of Cu length on the magnetic behaviour of Fe/Cu multi-segmented nanowires, *Nanomaterials*, 2018, **8**(7), 490.
8 A. Ruiz-Clavijo, O. Caballero-Calero and M. Martín-González, Three-dimensional Bi_2Te_3 networks of interconnected nanowires: synthesis and optimization, *Nanomaterials*, 2018, **8**(5), 345.
9 O. Caballero-Calero and M. Martín-González, 3D porous alumina: a controllable platform to tailor magnetic nanowires, in *Magnetic Nano- and Microwires*, 2020, Elsevier, pp. 3–20.
10 A. Ganapathi, P. Swaminathan and L. Neelakantan, Anodic aluminum oxide template assisted synthesis of copper nanowires using a galvanic displacement process for electrochemical denitrification, *ACS Appl. Nano Mater.*, 2019, **2**(9), 5981–5988.
11 X. Zheng, *et al.*, Large-scale pattern transfer based on non-through-hole AAO self-supporting membranes, *Nanotechnology*, 2020, **31**(19), 195301.
12 J.-L. Tian, *et al.*, Large-scale preparation of uniform nanopatterned silicon substrates by inductively coupled plasma etching using self-assembled anodic alumina masks, *ECS J. Solid State Sci. Technol.*, 2016, **5**(6), 320.
13 P. Alonso-González, *et al.*, Ordered InAs QDs using prepatterned substrates by monolithically integrated porous alumina, *J. Cryst. Growth*, 2006, **294**(2), 168–173.

14 M. Salaheldeen, *et al.*, Tuning nanohole sizes in Ni hexagonal antidot arrays: large perpendicular magnetic anisotropy for spintronic applications, *ACS Appl. Nano Mater.*, 2019, **2**(4), 1866–1875.
15 Z. Zeng, *et al.*, Fabrication of graphene nanomesh by using an anodic aluminum oxide membrane as a template, *Adv. Mater.*, 2012, **24**(30), 4138–4142.
16 J. A. Perez-Taborda, *et al.*, Ultra-low thermal conductivities in large-area Si–Ge nanomeshes for thermoelectric applications, *Sci. rep.*, 2016, **6**, 32778.
17 B. Tzaneva, *et al.*, Cobalt electrodeposition in nanoporous anodic aluminium oxide for application as catalyst for methane combustion, *Electrochim. Acta*, 2016, **191**, 192–199.
18 M. Nie, *et al.*, Co–Ni nanowires supported on porous alumina as an electrocatalyst for the hydrogen evolution reaction, *Electrochem. Commun.*, 2020, 106719.
19 J. Carneiro, *et al.*, The influence of the morphological characteristics of nanoporous anodic aluminium oxide (AAO) structures on capacitive touch sensor performance: a biological application, *RSC Adv.*, 2018, **8**(65), 37254–37266.
20 I. Vlassiouk, *et al.*, "Direct" detection and separation of DNA using nanoporous alumina filters, *Langmuir*, 2004, **20**(23), 9913–9915.
21 U. Malinovskis, *et al.*, High-density plasmonic nanoparticle arrays deposited on nanoporous anodic alumina templates for optical sensor applications, *Nanomaterials*, 2019, **9**(4), 531.
22 A. Ruiz-Clavijo, *et al.*, Tailoring magnetic anisotropy at will in 3D interconnected nanowire networks, *Phys. Status Solidi RRL*, 2019, **13**(10), 1900263.
23 O. Caballero-Calero and M. Martín-González, Thermoelectric nanowires: a brief prospective, *Scr. Mater.*, 2016, **111**, 54–57.
24 M. M. Rojo, *et al.*, Thermal conductivity of Bi_2Te_3 nanowires: how size affects phonon scattering, *Nanoscale*, 2017, **9**(20), 6741–6747.
25 F. Domínguez-Adame, *et al.*, Nanowires: a route to efficient thermoelectric devices, *Phys. E*, 2019, **113**, 213–225.
26 J. Martín, A. Nogales and M. Martín-González, The smectic–isotropic transition of P_3HT determines the formation of nanowires or nanotubes into porous templates, *Macromolecules*, 2013, **46**(4), 1477–1483.
27 J. Lee, *et al.*, Thermal conductivity of anodized aluminum oxide layer: the effect of electrolyte and temperature, *Mater. Chem. Phys.*, 2013, **141**(2–3), 680–685.
28 D.-A. Borca-Tasciuc and G. Chen, Anisotropic thermal properties of nanochanneled alumina templates, *J. Appl. Phys.*, 2005, **97**(8), 084303.
29 A. Cai, *et al.*, Thermal conductivity of anodic alumina film at (220 to 480) K by laser flash technique, *J. Chem. Eng. Data*, 2010, **55**(11), 4840–4843.
30 B. A. Abad, J. Maiz and M. Martin-Gonzalez, Rules to determine thermal conductivity and density of Anodic Aluminum Oxide (AAO) membranes, *J. Phys. Chem. C*, 2016, **120**(10), 5361–5370.
31 M. Muñoz Rojo, *et al.*, Fabrication of Bi_2Te_3 nanowire arrays and thermal conductivity measurement by 3ω-scanning thermal microscopy, *J. Appl. Phys.*, 2013, **113**(5), 054308.
32 G. A. Slack, Thermal Conductivity of MgO, Al_2O_3, $MgAl_2O_4$, and Fe_3O_4 Crystals from 3° to 300° K, *Phys. Rev.*, 1962, **126**(2), 427.
33 M. McQuarrie, Thermal conductivity: VII, analysis of variation of conductivity with temperature for Al_2O_3, BeO, and MgO, *J. Am. Ceram. Soc.*, 1954, **37**(2), 91–95.
34 R. Williams, *et al.*, The effects of Cr_2O_3 and Fe_2O_3 additions on the thermal conductivity of Al_2O_3, *J. Appl. Phys.*, 1987, **61**(10), 4894–4901.
35 T. Ogden, A. Rathsam and J. Gilchrist, Thermal conductivity of thick anodic oxide coatings on aluminum, *Mater. Lett.*, 1987, **5**(3), 84–87.
36 J. C. Lambropoulos, *et al.*, Thermal conductivity of dielectric thin films, *J. Appl. Phys.*, 1989, **66**(9), 4230–4242.
37 I. Stark, M. Stordeur and F. Syrowatka, Thermal conductivity of thin amorphous alumina films, *Thin Solid Films*, 1993, **226**(1), 185–190.
38 S.-M. Lee, D. G. Cahill and T. H. Allen, Thermal conductivity of sputtered oxide films, *Phys. Rev. B: Condens. Matter Mater. Phys.*, 1995, **52**(1), 253.
39 D. G. Cahill, S.-M. Lee and T. I. Selinder, Thermal conductivity of κ-Al_2O_3 and α-Al_2O_3 wear-resistant coatings, *J. Appl. Phys.*, 1998, **83**(11), 5783–5786.
40 L. Braginsky, *et al.*, High-temperature thermal conductivity of porous Al_2O_3 nanostructures, *Phys. Rev. B: Condens. Matter Mater. Phys.*, 2004, **70**(13), 134201.
41 M. M. Rojo, *et al.*, Decrease in thermal conductivity in polymeric P_3HT nanowires by size-reduction induced by crystal orientation: new approaches towards thermal transport engineering of organic materials, *Nanoscale*, 2014, **6**(14), 7858–7865.
42 B. Abad, D.-A. Borca-Tasciuc and M. Martin-Gonzalez, Non-contact methods for thermal properties measurement, *Renewable Sustainable Energy Rev.*, 2017, **76**, 1348–1370.
43 B. Abad, *et al.*, Tailoring thermal conductivity *via* three-dimensional porous alumina, *Sci. Rep.*, 2016, **6**, 38595.
44 M. Mata-Zamora and J. Saniger, Thermal evolution of porous anodic aluminas: a comparative study, *Rev. Mex. Fis.*, 2005, **51**(5), 502–509.
45 N. Sirota and G. Shokhina, Kinetics of polymorphous transformations of anodic alumina, *Krist. Tech.*, 1974, **9**(8), 913–919.
46 L. Vera-Londono, *et al.*, Advances in scanning thermal microscopy measurements for thin films, in *Coatings and Thin-Film Technologies*, IntechOpen, 2018, pp. 3–14.
47 M. M. Rojo, *et al.*, Decrease in thermal conductivity in polymeric P_3HT nanowires by size-reduction induced by crystal orientation: new approaches towards thermal transport engineering of organic materials, *Nanoscale*, 2014, **6**(14), 7858–7865.
48 I. Horcas, *et al.*, WSXM: a software for scanning probe microscopy and a tool for nanotechnology, *Rev. Sci. Instrum.*, 2007, **78**(1), 013705.

49 A. A. Wilson, *et al.*, Thermal conductivity measurements of high and low thermal conductivity films using a scanning hot probe method in the 3ω mode and novel calibration strategies, *Nanoscale*, 2015, **7**(37), 15404–15412.
50 K. Chernyakova, *et al.*, Structural and fluorescence studies of polycrystalline α-Al_2O_3 obtained from sulfuric acid anodic alumina, *Phys. Status Solidi A*, 2018, **215**(16), 1700892.
51 C. Manzano, *et al.*, The influence of thickness, interpore distance and compositional structure on the optical properties of self-ordered anodic aluminum oxide films, *J. Mater. Chem. C*, 2016, **4**(32), 7658–7666.
52 K. Tomikawa and H. Kanno, Raman study of sulfuric acid at low temperatures, *J. Phys. Chem. A*, 1998, **102**(30), 6082–6088.
53 T. Assih, *et al.*, Raman study of alumina gels, *J. Mater. Sci.*, 1988, **23**(9), 3326–3331.
54 G. Mariotto, *et al.*, Raman and X-ray diffraction study of boehmite gels and their transformation to α- or β-alumina, *J. Solid State Chem.*, 1990, **86**(2), 263–274.
55 W. Xu, *et al.*, Effects of high-temperature annealing on structural and optical properties of highly ordered porous alumina membranes, *Appl. Phys. Lett.*, 2004, **85**(19), 4364–4366.
56 S. Porto and R. Krishnan, Raman effect of corundum, *J. Chem. Phys.*, 1967, **47**(3), 1009–1012.
57 Y. Ma, *et al.*, IR and Raman investigation of one-dimensional and three-dimensional aluminophosphite, *J. Phys. Chem. C*, 2007, **111**(49), 18361–18366.
58 A. Goullet, *et al.*, Polarization dependence of the first-order Raman spectrum of α-$AlPO_4$, *Phys. Rev. B: Condens. Matter Mater. Phys.*, 1991, **44**(18), 9936.
59 B. Lafuente, R. T. Downs, H. Yang and N. Stone, *Highlights in Mineralogical Crystallography, RRUFF Database*, ed. T. Armbruster and R. M. Danisi, Berlin, Germany, 2015, pp. 1–30.
60 L. Fernández-Romero, *et al.*, Assessment of the thermal stability of anodic alumina membranes at high temperatures, *Mater. Chem. Phys.*, 2008, **111**(2–3), 542–547.
61 I. Brown, *et al.*, Structural and thermal characterisation of nanostructured alumina templates, *Curr. Appl. Phys.*, 2006, **6**(3), 557–561.